Dynamic Conductivity of Molten Salts

Part I: $3\,KNO_3 \cdot 2\,Ca(NO_3)_2$ at Frequencies from 100 MHz to 40 GHz

K. Funke, J. Hermeling*, and J. Kümpers

Institut für Physikalische Chemie der Westfälischen Wilhelms-Universität Münster, 4400 Münster, and Sonderforschungsbereich 173, Federal Republic of Germany

Z. Naturforsch. **43a**, 1094–1102 (1988); received September 13, 1988

The dynamic ionic conductivity of the molten salt $3\,KNO_3 \cdot 2\,Ca(NO_3)_2$ has been measured at frequencies from 100 MHz to 40 GHz, at temperatures between 422 K and 478 K. Coaxial and rectangular waveguide systems have been used at 0.1 to 18 GHz and at 18 to 40 GHz, respectively. The conductivity is found to display the dispersion that is characteristic of the so-called "universal dielectric response". A similar dispersion was observed earlier at lower temperatures and frequencies. The data form arcs in the complex conductivity plane, with centers below the real axis. The modulus representation turns out to be comparatively involved and indirect, M'' featuring two maxima, while the conductivity data traverse a single arc in the complex plane. The present results are interpreted in terms of a non-Debye jump-relaxation model involving only one reorientational relaxation time. This time and its temperature dependence are close to those derived from other techniques.

Introduction

The glass forming molten salt $3\,KNO_3 \cdot 2\,Ca(NO_3)_2$ is a simple ionic system with interesting dynamic properties. Relaxation-type processes have been observed by different techniques in this material, including longitudinal [1] and transverse [2, 3] ultrasonic studies as well as Brillouin scattering [4, 5] and electrical relaxation [6] measurements. The (mean) conductivity and shear relaxation times have been found to vary by about 10 and 14 orders of magnitude, respectively, if the temperature is changed from 330 to 650 K [6, 7].

In $3\,KNO_3 \cdot 2\,Ca(NO_3)_2$, the glass transformation range extends roughly from 330 to 360 K [7–9]. Within this range, the system is known to show the characteristic features of the so-called "universal dielectric response" [10], comprising in particular the transition from a well-defined low-frequency conductivity to a power-law behavior of the electrical conductivity, $\sigma \propto \omega^p$, which is observed at sufficiently high frequencies. The existing data [6], see Fig. 1, are limited to frequencies $\nu = \omega/2\pi < 1$ MHz.

The shape of $\sigma(\omega)$ has been described by considering a distribution of relaxation times [6, 7, 11] and by introducing a fractional exponential relaxation function [6, 7, 11, 12]. The data have often been presented in terms of the complex dielectric modulus, $\hat{M} = M' + iM'' = \hat{\varepsilon}^{-1} = (\varepsilon' - i\varepsilon'')^{-1}$, see [12, 13, 6, 7], or by use of the normalized complex modulus, $\hat{N}$, which is related to $\hat{M}$ via $\hat{N}(\omega) = \hat{M}(\omega)/M'(\infty)$. It should, however, be pointed out that the above formal de-

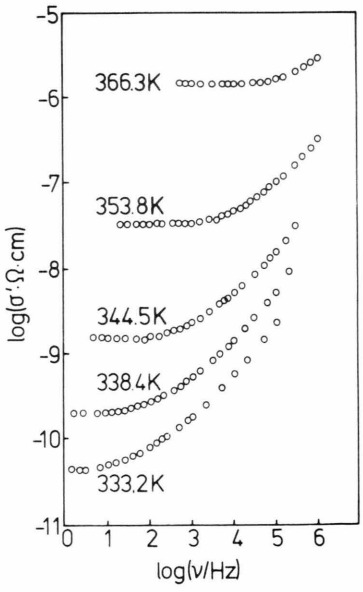

Fig. 1. Low-frequency conductivity dispersion of $3\,KNO_3 \cdot 2\,Ca(NO_3)_2$ at 333 K to 366 K, according to [6].

* Present address: Institut für Physikalische Chemie der Gesamthochschule Siegen, 5900 Siegen, FRG.

Reprint requests to Prof. Dr. K. Funke, Institut für Physikalische Chemie, SFB 173, Universität Münster, D-4400 Münster.

0932-0784 / 88 / 1200-1094 $ 01.30/0. – Please order a reprint rather than making your own copy.

scriptions are merely convenient empirical ways of representation. A priori, they do not provide any insight into the actual microscopic relaxation process.

The technique of Brillouin scattering has been applied to analyze the structural relaxation in molten $3\,KNO_3 \cdot 2\,Ca(NO_3)_2$ in the high-temperature, high-frequency regime [4, 5]. The spectra yield the temperature dependence of the velocity and attenuation of sound waves at frequencies of about 10 GHz. The modulus representation has been used to discuss the data. It has been concluded that – in terms of the normalized complex longidutinal modulus, $\hat{N}_l$, – a single relaxation time, τ, is sufficient to describe the relaxation in the melt, at least at temperatures above ca. 473 K [7]. At these temperatures, the imaginary part of $\hat{N}_l(\omega)$ should accordingly be given by the simple expression

$$N_l''(\omega) = \frac{\omega\tau}{1+(\omega\tau)^2}\,. \tag{1}$$

In Fig. 2 we reproduce a plot of this function, at 500 K, from [7]. Figure 2 also shows the measured frequency dependence of N_l'' at 399 K as obtained from ultrasonic data [1], see also [7]. If (1) is valid and if, moreover, $\hat{N}$ and $\hat{N}_l$ are assumed to be identical or similar functions of frequency, cf. [7], this implies that the dynamic conductivity, $\sigma(\omega)$, should be constant or approximately constant, showing no pronounced dispersion up to millimeter-wave frequencies or beyond. Also, on the basis of Fig. 2, the shape of $N''(\omega)$ might be expected to exhibit a gradual change within the temperature range from 400 to 500 K, approaching the form of (1) in a rather continuous fashion.

In our present study we have measured the dynamic conductivity of molten $3\,KNO_3 \cdot 2\,Ca(NO_3)_2$ at radio and microwave frequencies in order to test the validity of the above assumptions and, more generally, to learn more about the short-time relaxation processes in this material. In the following we will show that even at 478 K the conductivity is found to display the typical dispersion already known from the low-temperature, low-frequency conductivity spectra of Figure 1. Furthermore, the shape of $M''(\log \nu)$ does *not* continuously change from a broad asymmetric distribution to a relatively narrow symmetric bell-shaped curve, see Fig. 2, as the temperature is increased above 400 K. Instead, at temperatures around 450 K, $M''(\log \nu)$ is found to have *two* maxima, cf. Fig. 12, while the conductivity traverses a single arc in the complex plane.

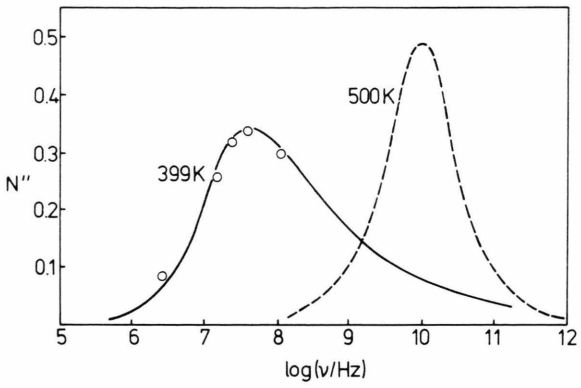

Fig. 2. Imaginary part of the normalized longitudinal modulus of $3\,KNO_3 \cdot 2\,Ca(NO_3)_2$. The ultrasonic data taken at 399 K are from [1]. The narrow symmetric curve at 500 K corresponds to (1) and has been suggested by Angell and Torell [7].

Our present results will be interpreted in terms of a simple jump-relaxation model, which was originally designed for application in structurally disordered solid electrolytes. The relaxation processes described by the model are non-Debye in character, although only one reorientational relaxation time is involved. This time and its temperature dependence turn out to be close to those derived from the Brillouin scattering data [4, 5] and from the shear viscosity [2, 3].

Experimental

Samples were prepared from reagent grade chemicals. $Ca(NO_3)_2 \cdot 4\,H_2O$ was dehydrated in a vacuum chamber for four days, at temperatures increasing up to 220 °C. During the dehydration process, it was intermittently ground and analyzed gravimetrically. The KNO_3 was dried for two days, at temperatures increasing up to 180 °C. Aliquot amounts of $Ca(NO_3)_2$ and KNO_3 were dissolved in one another at 270 °C. The resulting clear melt of $3\,KNO_3 \cdot 2\,Ca(NO_3)_2$ was kept at 220 °C.

Figures 3 and 4 are block diagrams of the experimental set-ups used in the coaxial and rectangular waveguide regimes, respectively. In both measuring assemblies, an hp 8350 B sweep oscillator and an hp 8757 A scalar network analyzer are controlled by an hp 9000 (series 300) desk-top computer. The arrangements of Figs. 3 and 4 allow for fully automated swept measurements. The coaxial and rectan-

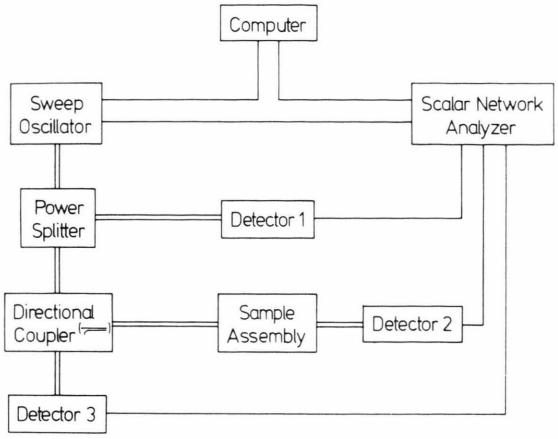

Fig. 3. Block diagram of experimental set-up in the coaxial-waveguide frequency range.

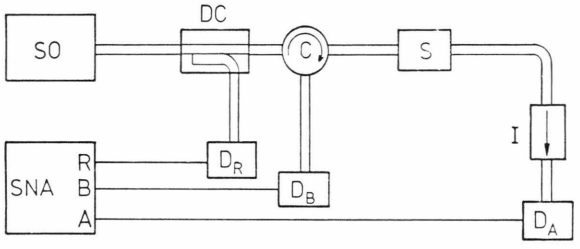

Fig. 4. Block diagram of experimental set-up in the rectangular-waveguide frequency range. SO: sweep oscillator; SNA: scalar network analyzer; DC: directional coupler; C: circulator; S: sample; I: isolator; D: detector.

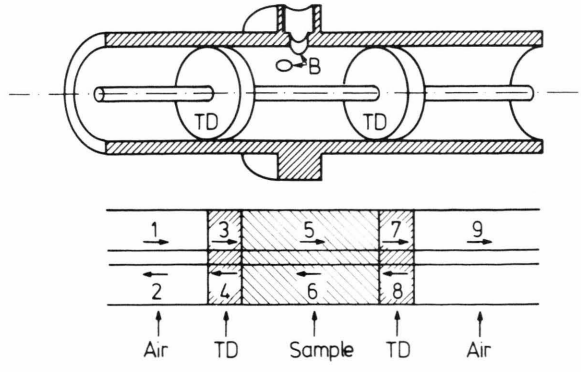

Fig. 5. Exploded view of coaxial-waveguide sample assembly and travelling waves in different media. TD: teflon disks; B: inlet borings for melt.

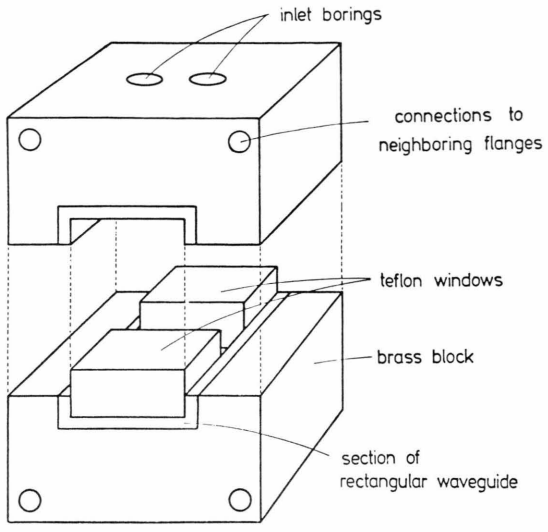

Fig. 6. Exploded view of rectangular-waveguide sample assembly.

gular assemblies shown in Figs. 3 and 4 have been used at frequencies ranging from 0.1 to 18 GHz and from 26.5 to 40 GHz, respectively. At K-band frequencies, from 18 to 26.5 GHz, the set-up of Fig. 4 was simplified by not including the isolator and by replacing the circulator by a 3 dB directional coupler.

The quantities measured are the absolute values of the complex transmission and reflection factors, $|\hat{t}|$ and $|\hat{r}|$, of the sample sections within the waveguide systems. Exploded views of the sample sections are shown in Figs. 5 and 6, for the coaxial and rectangular case, respectively. Figure 5 includes a schematic representation of the nine individual travelling waves in the various media, i.e., in air, in the window material (teflon, see Figs. 5 and 6), and in the molten salt itself. Let us denote the nine complex amplitudes of the respective electric fields by $\hat{E}_{01}$ to $\hat{E}_{09}$. The measured scalar quantities may now be written as

$$|\hat{t}| = |\hat{E}_{09}/\hat{E}_{01}| \tag{2}$$

and

$$|\hat{r}| = |\hat{E}_{02}/\hat{E}_{01}|. \tag{3}$$

The eight ratios, $\hat{E}_{02}/\hat{E}_{01}$ to $\hat{E}_{09}/\hat{E}_{01}$, are uniquely determined by the dielectric and electric properties of the materials involved and by the requirement that the transverse electric and magnetic field components be continuous at the interfaces. The continuity conditions give us a set of eight simultaneous complex equa-

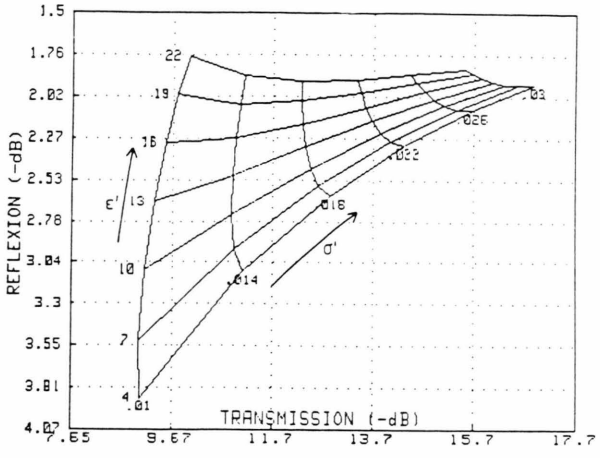

Fig. 7. A transformation network at 1.5 GHz (2 mm teflon disks, 10 mm sample); σ' is in $1/(\Omega\,\mathrm{cm})$.

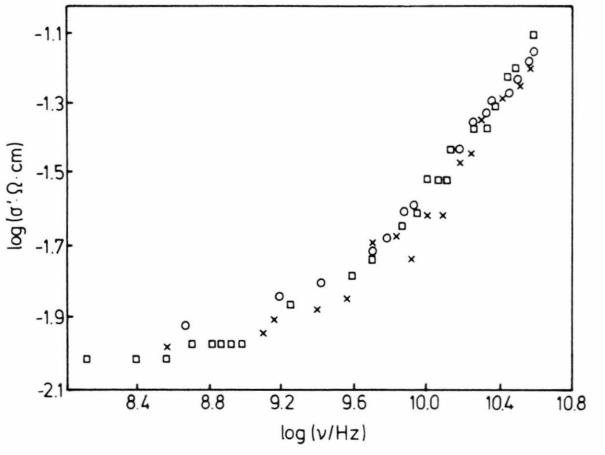

Fig. 8. Conductivity dispersion at 453 K as obtained from samples of different lengths.

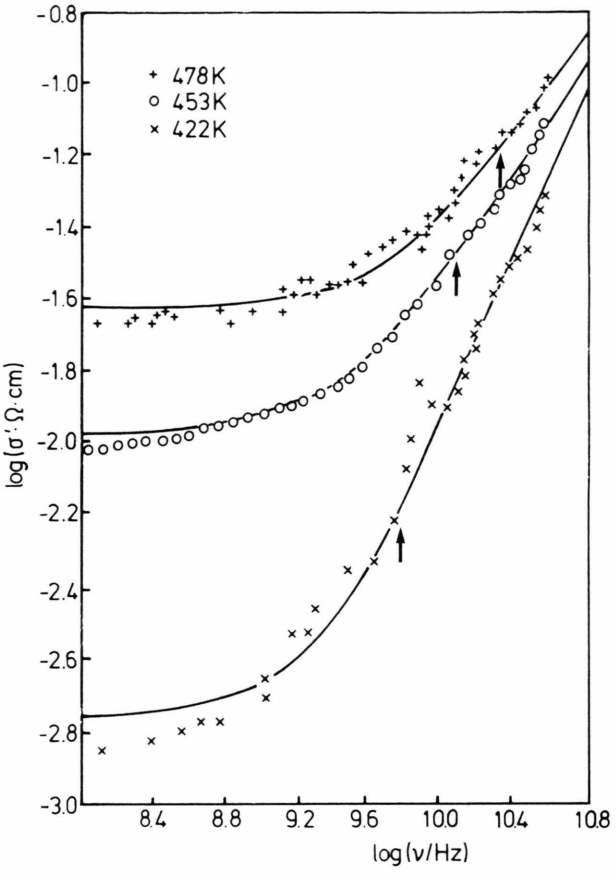

Fig. 9. Conductivity dispersion at temperatures from 422 K to 478 K. The solid lines have been claculated from our jump-relaxation-type model. The arrows mark the particular frequencies $\nu_{rr} = (2\pi\tau)^{-1}$.

tions which are linear in the eight rations, $\hat{E}_{02}/\hat{E}_{01}$ to $\hat{E}_{09}/\hat{E}_{01}$, but transcendental in the dielectric and electric properties of the sample. It is therefore not easily possible to compute the complex permittivity, $\hat{\varepsilon}(\omega)$, or the complex conductivity,

$$\hat{\sigma}(\omega) = \sigma'(\omega) + i\sigma''(\omega) = i\omega\varepsilon_0\hat{\varepsilon}(\omega), \tag{4}$$

directly from $|\hat{t}|$ and $|\hat{r}|$. The set of equations is, however, easily solved for the ratios, $\hat{E}_{02}/\hat{E}_{01}$ to $\hat{E}_{09}/\hat{E}_{01}$, if one assumes certain values of the real parts of $\hat{\varepsilon}$ and $\hat{\sigma}$, which are called ε' and σ'. Transformation networks,

$$(\sigma', \varepsilon') \leftrightarrow (|\hat{t}|, |\hat{r}|), \tag{5}$$

may thus be prepared, and this has been done for each frequency and different sample lengths. An example is shown in Figure 7. In the experiment both permittivity and conductivity of the sample are automatically read from the relevant network and immediately plotted as functions of the frequency. In some cases the transformation $(|\hat{t}|, |\hat{r}|) \rightarrow (\sigma', \varepsilon')$ turns out to be multivalued, so σ' and ε' cannot be read from the network in an unambiguous way. Such ambiguities are, however, easily removed by using a set of different sample lengths.

Results

Figure 8 is a log-log plot of the conductivity, σ', versus frequency at 453 K. The figure shows that dif-

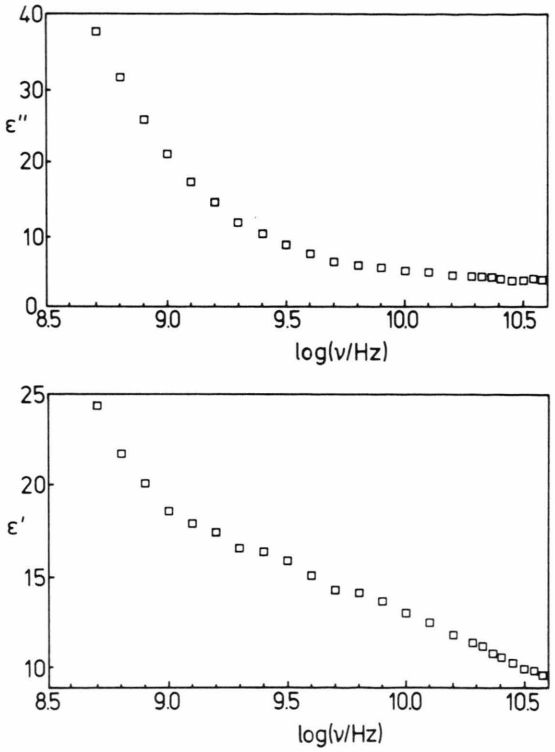

Fig. 10. Frequency dependence of ε'' and ε' at 453 K; experimental data.

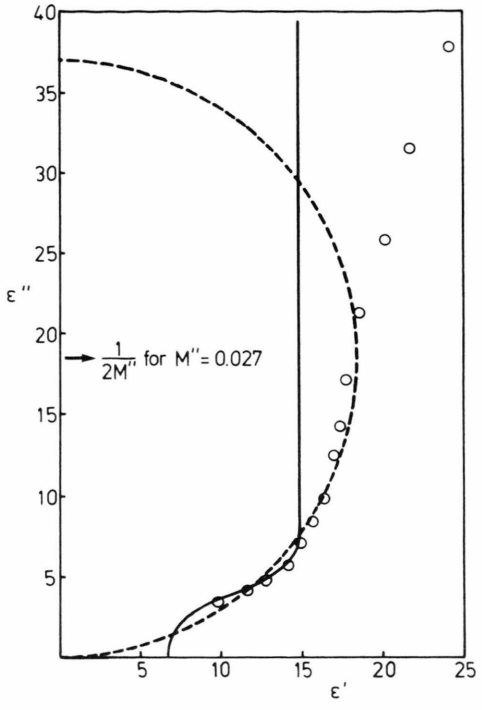

Fig. 11. Representation of experimental data at 453 K in the complex-permittivity plane. The solid line results from our model. Points of constant M'' form semicircles. The semicircle in the figure corresponds to $M'' = 0.027$.

ferent sample lengths yield consistent results. It also gives an impression of the scatter of the experimental data.

The mean values of the different 453 K runs are replotted in Fig. 9, together with data obtained at 422 K and at 478 K. It is evident that the spectra of Fig. 9 are similar to those of [6], see Fig. 1, and that trends already visible in the low-temperature results [6] are now continued: as the temperature is increased, the onset of the increase of $\sigma'(\nu)$ is shifted to higher frequencies; as a result, the formal activation energy turns out to be smaller in the power-law frequency range than it is in the limit of low frequencies.

The solid lines of Fig. 9 result from our model which will be outlined in the next section. At the present stage we note the following:

i) The general dependence of σ' on both frequency and temperature is very well reproduced by the model.

ii) An additional relaxation process seems to show up below 1 GHz, see especially the spectrum taken at 453 K. This process has not been considered in the model calculation.

The real and the imaginary part of the relative permittivity, $\varepsilon'(\nu)$ and $\varepsilon''(\nu)$, are both found to decrease continuously within the experimental frequency range. This is shown in Figure 10. In Fig. 11 we present a plot of $\varepsilon'' = \sigma'(\varepsilon_0 \omega)^{-1}$ versus ε' at 453 K. The figure contains experimental data as well as the result of our model calculation (solid line). The parameter values are as in Fig. 9, with $\varepsilon'(\infty) = 6.8$. Again, there is good agreement between model and experiment at sufficiently high frequencies, where ε' is smaller than 15. In the complex-permittivity plane, an arc-shaped feature extending from $\varepsilon' \approx 15$ down to $\varepsilon'(\infty)$ corresponds to the substantial increase of σ' observed at frequencies above 1 GHz. The existence of a non-zero low-frequency conductivity causes ε'' to increase as $1/\nu$ in the low-frequency limit. While the additional relaxation process not described in our present model calculation yields only a minor variation of conductivity below

1 GHz, the effect is much more dramatic in the permittivity plane, where we observe the corresponding variation of ε'.

The conventional way of representing frequency dependent electric and dielectric properties of materials is to do so in terms of conductivity and permittivity, see Figs. 9–11. Other ways of plotting the data are included in Figs. 12–15. The four different representations of Figs. 12–15 are all isotherms at 453 K. In each of these, the experimental data are shown along with a solid line which has been obtained from the model. The values of the model parameters are always the same as in Figs. 9 and 11.

In Fig. 12 the data of Fig. 11 are replotted in terms of the imaginary part of the dielectric modulus,

$$M'' = \frac{\varepsilon''}{\varepsilon'^2 + \varepsilon''^2}. \tag{6}$$

Featuring two separate maxima, the shape of $M''(\log \nu)$ differs from the expectations outlined in the introduction. We particularly note that $M''(\log \nu)$ is no longer a simple bell-shaped function and that there is no gradual narrowing of M'' as the temperature is increased from 400 to 500 K.

It is easy to visualize the reasons for the formation of two maxima of $M''(\log \nu)$ instead of one, if we reconsider Figure 11. In this figure, lines of constant M'' are semicircles with centers at $\varepsilon' = 0, \varepsilon'' = (2M'')^{-1}$ and radii $R = (2M'')^{-1}$. The particular semicircle for $M'' = 0.027$ is included in the figure. Now the criterion for the existence of two maxima of $M''(\log \nu)$ is that the line of $\varepsilon''(\varepsilon')$ should intersect at least one constant $-M''$ semicircle *four times*. This is indeed the case in the example of Figure 11. The low-frequency maximum of M'' would be even more pronounced, if the additional low-frequency relaxation did not exist, cf. the solid lines of Figs. 11 and 12.

Considering the fact that one relaxation process can create two maxima of $M''(\log \nu)$, we find the modulus representation more involved and indirect than the conventional representations. This point of view is emphasized by our Figs. 13–15, where the data are plotted in terms of conductivity and impedance and where the relaxation is described in a comparatively clear and simple manner.

In Fig. 13, the plot of Fig. 9 is extended to higher frequencies. According to the Kramers-Kronig relations and, more specifically, according to our model, the existence of a limiting value of the permittivity,

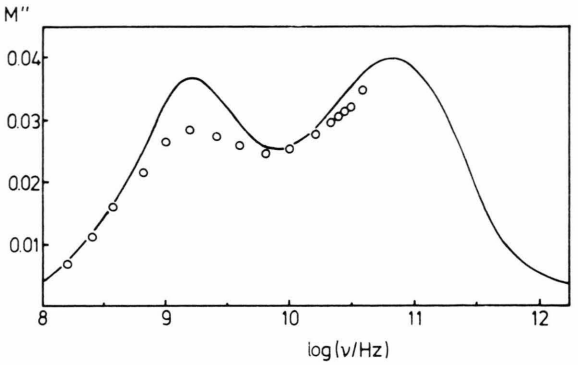

Fig. 12. Frequency dependence of M'' at 453 K; experimental data and model calculation.

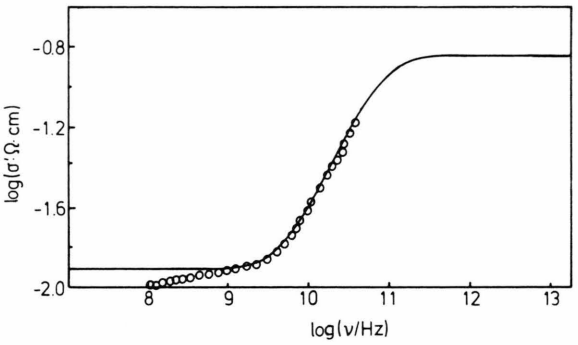

Fig. 13. Frequency dependence of σ' at 453 K; experimental data and model calculation.

$\varepsilon'(\infty)$, corresponds to the existence of a finite limiting value of the conductivity, $\sigma'(\infty)$. Figure 13 shows how the conductivity should gradually approach this value.

Figures 14 and 15 are plots of the complex planes of conductivity and impedance, respectively. As the value of $\varepsilon'(\infty)$ is not causally related to the relaxation, but due to faster processes, it is sensible not to include $\varepsilon'(\infty)$ in these representations. The plotted complex quantities have, therefore, been corrected for $\varepsilon'(\infty)$ in the following way:

$$\hat{\sigma}_{\text{relax}}(\omega) := \hat{\sigma}(\omega) - i\omega\varepsilon_o\varepsilon'(\infty), \tag{7}$$

$$\hat{Z}_{\text{relax}}(\omega) := 1/\hat{\sigma}_{\text{relax}}(\omega). \tag{8}$$

In both representations the model predicts the formation of almost circular arcs, with centers displaced below the real axes, see the solid lines of Figs. 14 and 15. Note that the arcs approach the real axes vertically.

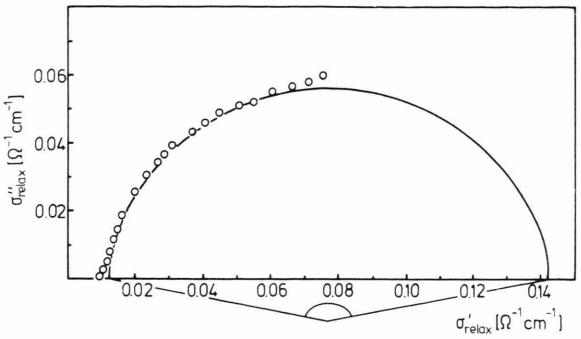

Fig. 14. Complex-conductivity arc at 453 K; experimental data and model calculation.

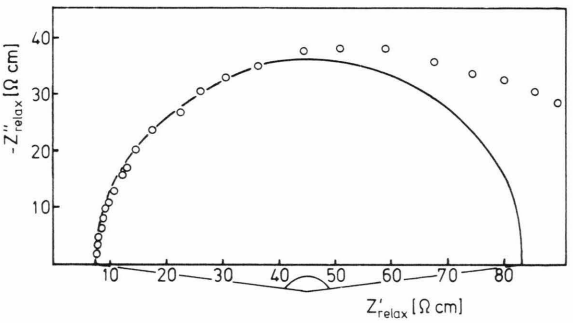

Fig. 15. Complex-impedance arc at 453 K; experimental data and model calculation.

In the complex-conductivity plane, the experimental points closely follow the calculated arc. There is a minor deviation at 40 GHz ($\sigma' \approx 0.08\ (\Omega\ \mathrm{cm})^{-1}$), due to characteristic experimental uncertainties at the Ka-band edge. On the other hand, the deviation at low frequencies and conductivities is a genuine property of $3\ KNO_3 \cdot 2\ Ca(NO_3)_2$. It is attributed to the above-mentioned additional relaxation process. At frequencies above 40 GHz, the validity of the calculated complex-conductivity arc will be checked by further measurements in the submillimeter-wavelength range. Clearly, the $\hat{\sigma}_{relax}$-representation is a particularly suitable and simple way of describing the relaxation process.

Due to the correction for $\varepsilon'(\infty)$ in (7) and (8), the high-frequency value of $\hat{Z}_{relax}$ is not zero, but the inverse of $\sigma'(\infty)$, see Figure 15. The experimental data closely follow the calculated $\hat{Z}_{relax}$-arc, except for the low-frequency regime, where the additional relaxation is now a substantial feature of its own.

Discussion

The dispersion observed in the molten salt $3\ KNO_3 \cdot 2\ Ca(NO_3)_2$ is of the general type found also in many other ionic and polaronic conductors including glassy and crystalline solid electrolytes. The characteristics of this type of dispersion comprise the power-law behavior of $\sigma'(\omega)$ and the formation of almost circular arcs with depressed centers in the complex planes of conductivity, impedance, and permittivity. The generality of the phenomenon was first noticed by Jonscher [10] who termed it "universal dielectric response".

Microscopically, an understanding of the "universal dielectric response" requires the solution of a complicated many-particle problem. A very general model was put forward by Ngai [14]. However, the model does not give a kinematic description of the microscopic dynamics. The same is true of other models that have been proposed [15].

More recently, a rather simple kinematic jump-relaxation model has been suggested by one of us [16–18]. It applies to any structurally disordered system of mobile charge carriers and is able to predict the main features of the "universal dielectric response". The solid lines of Figs. 9 and 11–15 have been calculated from this model. In addition to the lines, Fig. 9 also contains arrows marking particular frequencies. These are defined by

$$\nu_{rr} = \frac{1}{2\pi\tau}, \tag{9}$$

where τ is the reorientational relaxation time, see below. Compared with the relaxation time obtained from the shear viscosity and from Brillouin scattering [7], the present values are shorter roughly by a factor of five, but they have the same non-Arrhenius temperature dependence, see Figure 16.

The basic idea of the jump-relaxation model is sketched in Figure 17. In the figure, the momentary position of a mobile charge carrier (an ion) is denoted by A. The ion may hop to a neighboring position B, which requires some activation energy Δ. Now the model assumes that, if the ion resides at A, the neighborhood is structurally relaxed with respect to A. Therefore, the ion experiences a "conditional effective" single-particle potential which is normally higher at B than at A, see Figure 17a. As a consequence, the barrier height for a backward hop, δ, is smaller than Δ, at least immediately after the hop from A to B.

Suppose the ion hops from A to B at time $t = 0$. We then have to consider two competing relaxation processes at times $t > 0$:

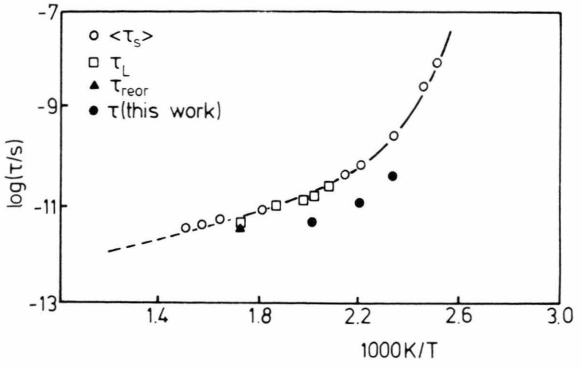

Fig. 16. Arrhenius plot of the reorientational relaxation time obtained from the present study, τ, the average shear relaxation time [7], $\langle\tau_S\rangle$, and the longitudinal relaxation time from Brillouin scattering [5, 7], τ_L. The reorientation time τ_{reor} is from Raman data [19].

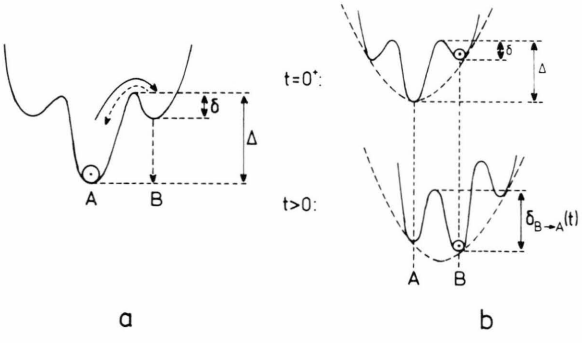

Fig. 17. Conditional effective potential and its development with time, see text.

i) The ion hops back to A. The correlated forward-backward hopping sequence thus performed contributes to the dynamic conductivity only at sufficiently high frequencies, but not at low frequencies.

ii) The neighborhood relaxes with respect to B. The reorientation of the neighborhood is characterized by some reorientational relaxation time, τ, and results in the formation of a new absolute minimum of the conditional effective potential at B. In this case the initial hop has eventually proved successful and thus contributes to the dc conductivity.

It is important to note that the backward barrier height, $\delta_{B\to A}(t)$, see Figure 17 b, increases as the ion stays at B. Therefore, the relaxation time of the back-hop process increases. The relaxation is thus slowed down as time progresses. The resulting spectra hence look as if there were a "distribution of relaxation times".

The model considers the probability, $W(t)$, that the correlated backward hop has not yet been performed at time t. A rate equation and simple geometrical arguments lead to a closed algebraic expression for $W(t)$, which makes use of the exponential-integral function [18]. A useful approximation is

$$W(t) \approx \exp\{-2A(1-\exp(-t/\tau))\cdot(\Delta-\delta)/kT\}, \quad (10)$$

where A is some constant of the order of one and τ is again the reorientational relaxation time of the neighborhood. The approximation of (10) is valid, if $(\Delta-\delta)/kT \lesssim 1$. Neglecting the finite duration of hops we may now construct the velocity autocorrelation function of the hopping motion,

$$\langle \boldsymbol{v}(0)\cdot\boldsymbol{v}(t)\rangle_{\text{hops}} = \text{const}\cdot\{\delta(t)+\dot{W}(t)\}, \quad (11)$$

where $\delta(t)$ is the delta function. The (frequency dependent) coefficient of self-diffusion is obtained from (11) by Fourier transformation, and the conductivity is formed with the help of the Nernst-Einstein relation. Cross terms are neglected. The procedure yields the expression

$$\hat{\sigma}_{\text{relax}}(\omega) = \left(1+\int_0^\infty \dot{W}(t)\exp(-i\omega t)\,dt\right) C/(\tau T). \quad (12)$$

The solid lines of Figs. 9 and 11–14 have been obtained with the following set of parameter values:

$$A = 1,$$
$$(\Delta-\delta) \approx k\cdot 550\ \text{K}\ \text{(slightly } T\text{-dependent)},$$
$$C = 8\cdot 10^{-10}\,(\text{Ks})/(\Omega\,\text{cm}). \quad (13)$$

Instead of (10) we have, however, used the respective expression given in [18]. The optimum values of the relaxation time τ are those plotted in Figure 16. Thus, from our present data we obtain a non-Arrhenius temperature dependence of τ. As noted before, this is in agreement with results from other techniques, see Figure 16. The temperature dependence of both the dc conductivity and the relaxation time shows that Δ has to be much larger than kT. Within our experimental temperature range, $\Delta \approx 10\,kT$ is a good estimate, again in agreement with [7]. The difference, $(\Delta-\delta)\approx k\cdot 550$ K, is thus found to be considerably smaller than the barrier heights, Δ and δ, themselves. Nevertheless it is this difference that causes the dispersion observed in the present study.

The charge carriers performing the correlated forward-backward hopping motion and thus causing the relaxation observed at frequencies above 1 GHz

are most probably the potassium ions. The additional relaxation found at lower frequencies is tentatively attributed to a similar behavior of the calcium ions.

Conclusions

The dynamic conductivity of the simple molten salt $3\,KNO_3 \cdot 2\,Ca(NO_3)_2$ has been determined in the radio and microwave frequency range up to 40 GHz. A pronounced dispersion has been detected. The shape of the frequency dependent conductivity is similar to the respective low-frequency data measured earlier in the glass-transformation temperature range [6]. The spectra bear the traits that are characteristic of the so-called "universal dielectric response". In favor of simplicity and clarity of representation it is proposed to display and discuss the data in terms of the complex conductivity rather than the dielectric modulus. The experimental results are shown to be consistent with a simple jump-relaxation model [16–18]. Application of the model yields a reorientational relaxation time with a non-Arrhenius temperature dependence.

Acknowledgements

We would like to thank R. Hoppe for his help with the numerical fitting procedure. Financial support from the Fonds der Chemischen Industrie is gratefully acknowledged.

[1] R. Weiler, R. Bose, and P. B. Macedo, J. Chem. Phys. **53,** 1258 (1970).
[2] H. Tweer, N. Laberge, and P. B. Macedo, J. Amer. Ceram. Soc. **54,** 121 (1971).
[3] G. M. Glover and A. J. Matheson, Trans. Faraday Soc. **67,** 1960 (1971).
[4] L. M. Torell, J. Chem. Phys. **76,** 3467 (1982).
[5] L. M. Torell and R. Aronsson, J. Chem. Phys. **78,** 943 (1983).
[6] F. S. Howell, R. A. Bose, P. B. Macedo, and C. T. Moynihan, J. Phys. Chem. **78,** 639 (1974).
[7] C. A. Angell and L. M. Torell, J. Chem. Phys. **78,** 937 (1983).
[8] K. J. Rao, D. B. Helphrey, and C. A. Angell, Phys. Chem. Glasses **14,** 26 (1973).
[9] J. Wong and C. A. Angell, Glass: Structure by Spectroscopy, Dekker, New York 1976, Chapter 11.
[10] A. K. Jonscher, Nature, London **267,** 673 (1977).
[11] C. T. Moynihan, L. P. Boesch, and N. L. Laberge, Phys. Chem. Glasses **14,** 122 (1973).
[12] G. Williams and D. C. Watts, Trans. Faraday Soc. **66,** 80 (1970).
[13] P. B. Macedo, C. T. Moynihan, and R. Bose, Phys. Chem. Glasses **13,** 171 (1972).
[14] K. L. Ngai, Solid State Ionics **5,** 27 (1981).
[15] L. A. Dissado and R. M. Hill, Solid State Ionics **22,** 331 (1987) and references cited therein.
[16] K. Funke, Solid State Ionics **18/19,** 183 (1986).
[17] K. Funke, in: Superionic Solids and Solid Electrolytes: Recent Trends (A. L. Laskar and S. Chandra, eds.). Academic Press, New York 1988.
[18] K. Funke, Z. Phys. Chem. N.F. **154,** 251 (1987).
[19] J. H. R. Clarke and S. Miller, Chem. Phys. Lett. **13,** 97 (1972).